



Investigation of Stress Corrosion Cracking Initiation in Machined 304 Austenitic Stainless Steel in Magnesium Chloride Environment

Wenqian Zhang, Huanchun Wu, Siyang Wang, Yujin Hu, Kewei Fang, and Xuelin Wang

(Submitted June 10, 2019; in revised form December 15, 2019; published online January 14, 2020)

The effect of the machining-induced residual stresses and microstructural changes on the stress corrosion cracking (SCC) initiation in 304 austenitic stainless steel was investigated. The residual stress was measured with an x-ray diffractometer, and the microstructural changes were characterized by the electron backscatter diffraction. Through a load-free testing in the boiling magnesium chloride solution, the subsurface zone of high SCC sensitivity was identified by detecting the depth of the micro-cracks. The development of the SCC micro-crack was related to the machining-induced residual stresses and microstructural changes. The results showed that the SCC micro-crack was prone to propagate in the subsurface where the residual stress was larger than 200 MPa, along with high-density grain boundary. Additionally, the SCC micro-crack initiation was observed to develop along the machining-induced slip bands.

Keywords austenitic stainless steel, machining, microstructural changes, residual stress, stress corrosion cracking

1. Introduction

Austenitic stainless steels (ASSs) are the most used structural materials in nuclear power plants due to an excellent combination of the mechanical properties and corrosion resistance (Ref 1). However, ASSs can suffer from the stress corrosion cracking (SCC) in chloride-containing aqueous environments (Ref 2-4). Mechanical machining, one of the mostly used manufacturing technics, can alter the material surface integrity (SI), including the surface morphology, micro-hardness, residual stress/strain and microstructure (Ref 5). However, it has been reported that the machining operations significantly aggravate the SCC susceptibility in ASSs (Ref 6-9) as a result of machining-induced surface alterations (Ref 10-12). The SCC micro-crack initiation on the machined surface as well as in the subsurface, causing damage to the components' mechanical properties and corrosion resistance, may further result in catastrophic structural failures. Thus, there has been a significant research interest for the study of the SCC performance of the machined surface in the last few years (Ref 13-15). Improved understanding of the SCC performance on the

machined surface requires a realistic description of the relation between the SCC micro-crack initiation as well as residual stress distribution and key microstructure attributes.

Residual tensile stress is one of the major factors contributing to the SCC initiation on the machined surface (Ref 14, 16). Zhou et al. (Ref 17) explored the effect of the grinding-induced residual stress on the SCC initiation of 304L ASS. The study concluded that the residual tensile stress in the grinding direction enhanced the susceptibility to SCC, while the residual compressive stress in the perpendicular direction improved the SCC resistance. Rhouma et al. (Ref 18) also reported that the surfaces with the residual compressive stress had a negative impact on the SCC initiation of 316L ASS. In our previous investigation (Ref 14), a critical residual stress value of 190 MPa was reported for the SCC initiation on the machined surface of 316 ASS, and the residual stress value was noted to have a strong correlation with the micro-crack density. Zhou et al. (Ref 17) observed that the crack arrest occurred with the micro-cracks growing into a region with low or no tensile residual stresses. However, the relation between the residual stress and SCC micro-crack growth in the machined subsurface still lacks quantitative insights.

Microstructural changes also play a dominating role in the SCC propagation (Ref 8, 19, 20). The machining-induced microstructural changes include grain orientation alteration, grain refinement, new produced grain or sub-grain boundaries, dislocation and phase transformation, etc. (Ref 21). Ghosh et al. (Ref 10) studied the effect of the microstructural changes on the SCC susceptibility in machined 304L ASS. The study revealed that the surface machining resulted in an extensive grain refinement and strain-induced martensite transformation near the surface. The presence of high-density martensite resulted in a higher SCC susceptibility as the martensite dissolution rate in the corrosive environment was much higher than that of austenite. Chang et al. (Ref 13) claimed that the ultrafine-grain layer introduced by machining increased the SCC resistance of the cold-worked 316L ASS. Besides, dislocation pile-ups play an important role in the SCC process (Ref 22). The dislocations

Wenqian Zhang, School of Mechanical Engineering, Hubei University of Technology, Wuhan 430068, People's Republic of China; and School of Mechanical Science and Engineering, Huazhong University of Science and Technology, Wuhan 430074, People's Republic of China; **Huanchun Wu** and **Kewei Fang**, Suzhou Nuclear Power Research Institute, Suzhou 215004, People's Republic of China; and **Siyang Wang**, **Yujin Hu**, and **Xuelin Wang**, School of Mechanical Science and Engineering, Huazhong University of Science and Technology, Wuhan 430074, People's Republic of China. Contact e-mail: wangxl@hust.edu.cn.

enhanced the local electrochemical activation and promoted the micro-crack initiation (Ref 23). Formed by the dislocation movements (Ref 24), the slip bands are the major manifestation of the plastic deformation in the machined subsurface of ASS (Ref 10, 21). Magnin et al. (Ref 25) reported that the localized slip of the {111} planes induced the cleavage, based on the SCC fractography analysis in 316 ASS. The micro-cleavage and local dissolution synergistically induced the SCC advance on the crystal planes (Ref 22). In addition, Turnbull et al. (Ref 6) observed that the micro-cracks developed parallel to the slip lines in 304 ASS. However, the correlation between the SCC micro-crack growth and machining-induced microstructural changes remains poorly understood.

The machined surface conditions result in the microstructural changes coupled with the residual stress/strain (Ref 21). However, few research studies are available concerning the synergistic effects of the machining-induced residual stress and microstructural attributes on the SCC propagation in machined ASS. Therefore, it is essential to relate the SCC behaviors with the coupled effects of the residual stress and microstructural changes. A deep understanding of the combined action of the residual stress and microstructural changes can help in improving the SCC resistance by controlling the processing parameters.

The purpose of this study is to explore the effect of machining-induced microstructural changes and residual stress on the SCC initiation. The SCC testing was conducted in boiling MgCl₂ solution. The specimens were prepared with varied processing parameters, thus introducing different microstructural changes and residual stress distributions in the machined subsurface. The residual stress values and microstructural parameters were correlated with the SCC micro-crack depth. The research reported in this study builds a comprehensive understanding about the role of the machining-induced microstructural changes and residual stress in the SCC micro-crack initiation process.

2. Material and Experimental Procedures

2.1 Material

The material used in this study was the solution annealed 304 ASS in tubular form, with inner and outer diameters of 39.0 and 60.5 mm, respectively. Table 1 presents the chemical composition of the tested material. The material was solution annealed at 1040 °C for 60 min, along with air quenching.

2.2 Specimen Preparation

Firstly, six annular blanks were preprocessed on the 304 tube with a grooving insert, as shown in Fig. 1(a). Subsequently, the orthogonal machining was carried out on each circular surface (marked with blue) by cylindrical turning on a

Table 1 Chemical composition of the AISI 304 stainless steel (wt.%)

C	Si	Mn	P	Mo	Cr	Ni	Fe
0.0389	0.446	0.675	0.0225	0.172	18.3	8.53	Balance

computer numerical control lathe. The applied cutting tool was a turning insert (Sandvik TM 2135) with 3 mm width. Six annular specimens were machined with the operational parameters listed in Table 2, respectively. Each annular specimen was machined with a new cutter without any flank wear. Following the machining procedure, the annular specimens were cut away from the pipe, as shown in Fig. 1(b).

Three directions were defined on the machined cylindrical surface (marked with red). The *x*, *y* and *z* denoted the cutting, transverse and depth directions, respectively. Furthermore, five small specimens, with a length of about 15 mm, were cut from each annular specimen. Two of these specimens were used for determining the residual stress distribution and microstructural changes, and the other three samples were prepared for SCC testing. These specimens were numbered as Ci-j, where *i* (*i* = 1-6) represented the machining condition of Ci and *j* (*j* = 1-5) represented the number of specimens in condition Ci.

In addition to the machined specimens, an additional specimen (C0) was prepared without machining for comparison. A block of 10 mm × 10 mm × 3.5 mm dimensions was initially cut by using the electrical discharge machining from the tube. Its surface of 10 mm × 10 mm dimensions was ground and polished by a machine Ecomet300/Automet300. Afterward, in order to remove the hardened layer introduced by the mechanical grinding, the surface was further electro-polished with a mixed solution of perchloric acid (10%) and ethanol (90%). The electro-polishing process was conducted using an automatic twin-jet electropolisher (Struers, TenuPol-5) at 20 °C for 25 s, employing an operating voltage of 25 V.

2.3 Examination of Residual Stresses and Microstructure

After the cutting procedure, the machining-induced residual stresses were measured with an x-ray diffractometer (Proto iXRD). In the present study, Mn-K α was used as the x-ray radiation source, and the austenite peak of the crystal plane (311) was set to be the diffraction peak. The voltage and current applied for the test were 20 kV and 4 mA, respectively. The diffraction signals were acquired by two probes, which were analyzed with the $\sin^2\psi$ method in the iso-inclination mode. For this, seven iso-inclination angles were applied at 25°, 13.6°, 7.5°, 0°, -7.5°, -13.6° and -25°.

Two residual stress measurements were performed on the machined surface of the specimens Ci-1. One was conducted in the cutting direction (*x*), whereas the other was in the transverse direction (*y*). In addition to the surface measurements, the residual stresses in the cutting direction at different depths were also measured. To obtain the residual stress profile in the subsurface, successive layers of the material were removed by electro-polishing (Ref 26, 27). For each polishing operation, a layer of about 3-5 μ m thickness was stripped. The potential residual stress relaxation caused by the electro-polishing was not considered. For the specimen C1-1, the residual stress measurement was terminated as the machining-induced residual stress became insignificant. For other five specimens Ci-1 (*i* = 2-6), the residual stress measurement was terminated as the tensile residual stress decreased to about 0 MPa. It is considered that the residual stress was uniformly distributed along the circumference for the annular specimen processed by the orthogonal turning. Therefore, the acquired results for specimens Ci-1 represented the residual stress distribution of the machining condition Ci.

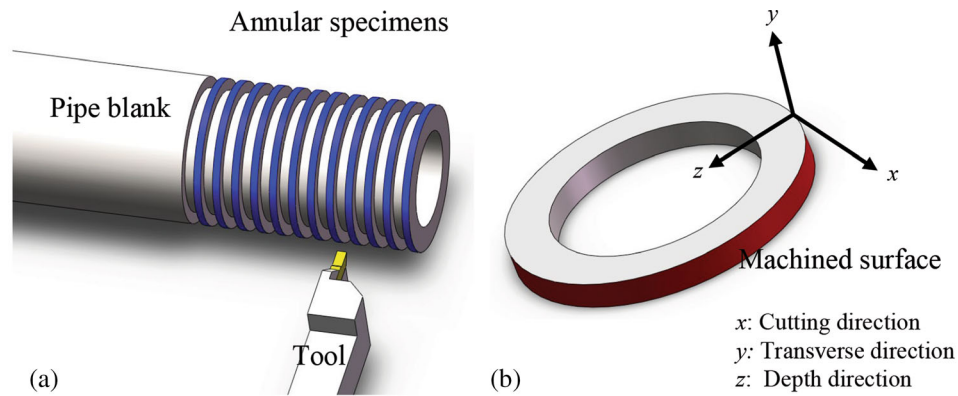


Fig. 1 (a) Schematic diagram showing orthogonal cutting process for the annular specimens. (b) Three defined directions on the machined cylindrical surface

Table 2 Cutting parameters for sample preparation

Condition	Cutting speed, m/min	Cutting depth, mm	Cutting width, mm
C1	35	0.10	3
C2	35	0.05	3
C3	60	0.05	3
C4	110	0.05	3
C5	110	0.10	3
C6	110	0.20	2.5

The machining-induced microstructural changes were characterized using a high-resolution field emission scanning electron microscopy (FSEM, FEI SIRION 200). The specimens Ci-2 were sectioned to allow for the microstructural observation, and the cross section was mechanically grinded, polished and etched using aqua regia. Subsequently, the subsurface micromorphology was analyzed in the secondary electron (SE) mode.

After SEM inspection, the cross section of the samples was mechanically polished and electro-polished. EBSD measurements were carried out on the cross sections with FSEM, and the acquired EBSD data were analyzed using the Orientation Imaging Microscopy™ system of EDAX/TSL. The cleanup procedure, which consisted of the grain confidence index standardization and neighbor phase correlation, was applied to the raw EBSD data in the TSL software (Ref 28). In this procedure, the minimum grain tolerance angle of 5°, minimum grain size of 2 pixels and minimum confidence index (CI) $CI > 0.1$ were chosen (CI quantifies the reliability of the indexed pattern). The scan step size used for EBSD examination was 1 μm . The EBSD results, in terms of grain orientation, misorientation, grain boundary (GB) and phase composition, were obtained from the inverse pole figure (IPF) map, kernel average misorientation (KAM) map, GB map and phase map, respectively. The KAM level reflects the dislocation density (Ref 29). The GBs include low-angle grain (LAGB), transition angle grain (TAGB) and high-angle grain (HAGB) boundaries, which were identified with the misorientation ranges of 2-5°, 5-15° and $> 15^\circ$, respectively (Ref 21). Both LAGB and TAGB are considered as sub-grain boundaries. To characterize the microstructural alterations quantitatively, the GB density and KAM values were calculated along the subsurface (Ref 21). It should be mentioned that the phase composition in the present

study involved the machining-induced martensite, original austenite and residual ferrite.

In addition to the EBSD examination, transmission electron microscopy (TEM) was utilized to further examine the microstructural alterations in the top surface layer of the specimen C2-2. Focused ion beam (FIB) milling was applied for the preparation of the TEM sample (Ref 21), and the TEM examination was carried out using a field emission transmission electron microscope (FEI Tecnai G2 F30).

2.4 SCC Test and Micro-crack Examination

Based on ASTM G36 (Ref 30), the SCC testing was conducted in a saturated MgCl_2 solution boiling at $155.0 \pm 1.0^\circ\text{C}$. The test environment was prepared in accordance with the procedure reported in the previous study (Ref 14). About 800 mL of the MgCl_2 solution was prepared in a 2000-mL Erlenmeyer flask heated by a hotplate. With the solution kept boiling state at $155.0 \pm 1.0^\circ\text{C}$, the specimens Ci-3, Ci-4 and Ci-5 were exposed to the test environment for 30, 60 and 600 min, respectively. Besides, the specimen C0 was also exposed to the corrosion environment for 600 min. During the SCC testing, the temperature and concentration of the boiling MgCl_2 solution were kept constant by preventing the loss of condensate and water vapor by using a condenser cooling system.

After the SCC test, the machined surfaces of specimens Ci-3, Ci-4 and Ci-5 were examined with a digital microscope (Keyence VHX-1000C) to obtain the micro-crack morphology. In addition to the surface examination, the micro-cracks in the subsurface were also detected with FSEM, and the depth of each micro-crack was measured. Moreover, the subsurface micro-cracks in the specimens Ci-5 were further detected using

the EBSD technology. The detected areas were close to the machined surface and contained at least one micro-crack.

3. Results

3.1 Machining-induced Residual Stresses

Table 3 presents the results of the surface residual stresses and their standard deviations, indicating large tensile residual stresses in both x and y directions on the turned surface. Furthermore, the residual stress distributions along the depth are shown in Fig. 2. Figure 2(a) shows the residual stress profile of specimen C1-1, presenting a typical spoon-shaped distribution. The residual stress state varied from the tensile stress to the compressive stress. The maximum tensile stress was 1036 MPa on the outmost surface, while the maximum compressive stress was -151 MPa at a depth of 120 μm beneath the surface. Moreover, Fig. 2(b), (c), (d), (e) and (f) illustrates the residual stress profiles of other five machining conditions with respect to tensile stress.

3.2 Machining-induced Microstructural Changes

Figure 3 shows the subsurface micromorphology of the specimen C1-2. The slip bands in the machining-induced metamorphic layer were denser than the deeper zones. The slip line direction was noted to vary in different grains. As a result of the material deformation and dislocation motion, the slip band is an important indicator reflecting the plastic deformation of the austenitic stainless steel in the machining-induced metamorphic layer. Figure 3(b) illustrates the microstructure within 50 μm near the surface. It could be seen that GBs within 20 μm were not obvious, and the slip line density was much higher than that in deeper positions. Moreover, significant cross-slip phenomenon was observed in the subsurface, which indicated the appearance of multi-slip systems in the grain. The tendency of multi-slip motion decreased with the increase in depth.

The results of a detailed detection of the near-surface zone of the specimen C2-2 are shown in Fig. 4, in which the left-hand side corresponds to the machined surface. As shown in the FSEM images, the ultrafine-grain structure was observed in the top surface zone, which exhibited a distinct morphology as compared to the non-ultrafine structure on the right side. The thickness of the ultrafine-grain zone varied along the surface. Moreover, as shown in the TEM image in Fig. 4(b), the ultrafine-grains were highly distorted and disordered. The electron diffraction analysis showed a polycrystalline diffrac-

tion pattern, demonstrating the generation of ultrafine-grains on the top surface.

Figure 5 displays the EBSD results of the subsurface of the specimen C5-2. The four panels of the same detected zone are the IPF map, GB map, KAM map and phase map of the same detected zone. As shown in the IPF map, the crystal orientation varied significantly in the near-surface zone. The top surface layer consisted of numerous colored points, corresponding to the ultrafine-grain structure as shown in Fig. 4. As the depth increased, the extent of orientation variation was noted to gradually reduce. The orientation change in the near-surface zone indicated the crystal deformation. Besides, new grain and sub-grain boundaries were the other microstructural characteristics introduced by machining, which can be seen in the GB map. High fractions of GBs were observed in the near-surface zone within approx. 30 μm . The newly produced HAGBs demonstrated the fragmentation of grains, while the LAGBs and TAGBs signified that the grains were deformed or distorted. The KAM map presents a high gradient of local plastic deformation along the depth, showing that the local plastic deformation was non-uniformly distributed in the subsurface. The phase map illustrates the distribution of the machining-induced martensite. As shown in Fig. 5(d), the red area corresponded to austenite, while the green area corresponded to martensite and residual ferrite. The residual ferrite would generally exist along the original austenite boundaries. Thus, the component in green corresponded to martensite. The phase distribution revealed that the generation of martensite was concentrated in the top surface layer or along the slip bands.

Comparing the EBSD maps, the zones with significant orientation changes and newly produced GBs suffered a high level of local deformation. In such subsurface zones, the slip bands and martensite were noted to generate preferentially. The EBSD results demonstrated the high gradient microstructural changes along the machined subsurface.

3.3 Surface Micro-cracks

Figure 6(a), (b), (c) and (d) illustrates the typical surface morphology of the specimen Ci-3 ($i = 2, 4, 5$ and 6) which had been exposed to boiling MgCl_2 solution for 30 min. On the specimen surface, the machining marks indicated the x direction, and the perpendicular direction denoted the y direction. The corresponding surface residual stresses in the two directions are labeled in the figures. Micro-cracks were primarily initiated along the machining as well as perpendicular directions, thus forming a crisscrossing meshwork morphology on the surface. The length of the micro-cracks ranged from a few dozens of microns to hundreds of microns. In addition, on the surface of the specimen C0, which was exposed to the corrosion environment for 600 min, no micro-crack was observed.

3.4 Subsurface Micro-crack

Figure 7 and 8, respectively, shows the FSEM results of the specimens C2-3 and C1-3 depicting the subsurface SCC micro-cracks and surrounding microstructure. As shown in Fig. 7(a), the micro-crack was initiated on the machined surface and propagated through the ultrafine-grain zone which was about several microns deep. No micro-crack branch was observed in the ultrafine-grain zone. Moreover, Fig. 8 displays large zones exhibiting the micro-crack propagation in the subsurface. It was

Table 3 Surface residual stresses of conditions C1–C6

Specimen	Surface residual stress, MPa	
	Cutting direction, x	Transverse direction, y
C1-1	1036 \pm 38	986 \pm 39
C2-1	823 \pm 43	869 \pm 36
C3-1	731 \pm 34	876 \pm 33
C4-1	790 \pm 39	971 \pm 29
C5-1	847 \pm 37	1148 \pm 91
C6-1	988 \pm 47	1101 \pm 45

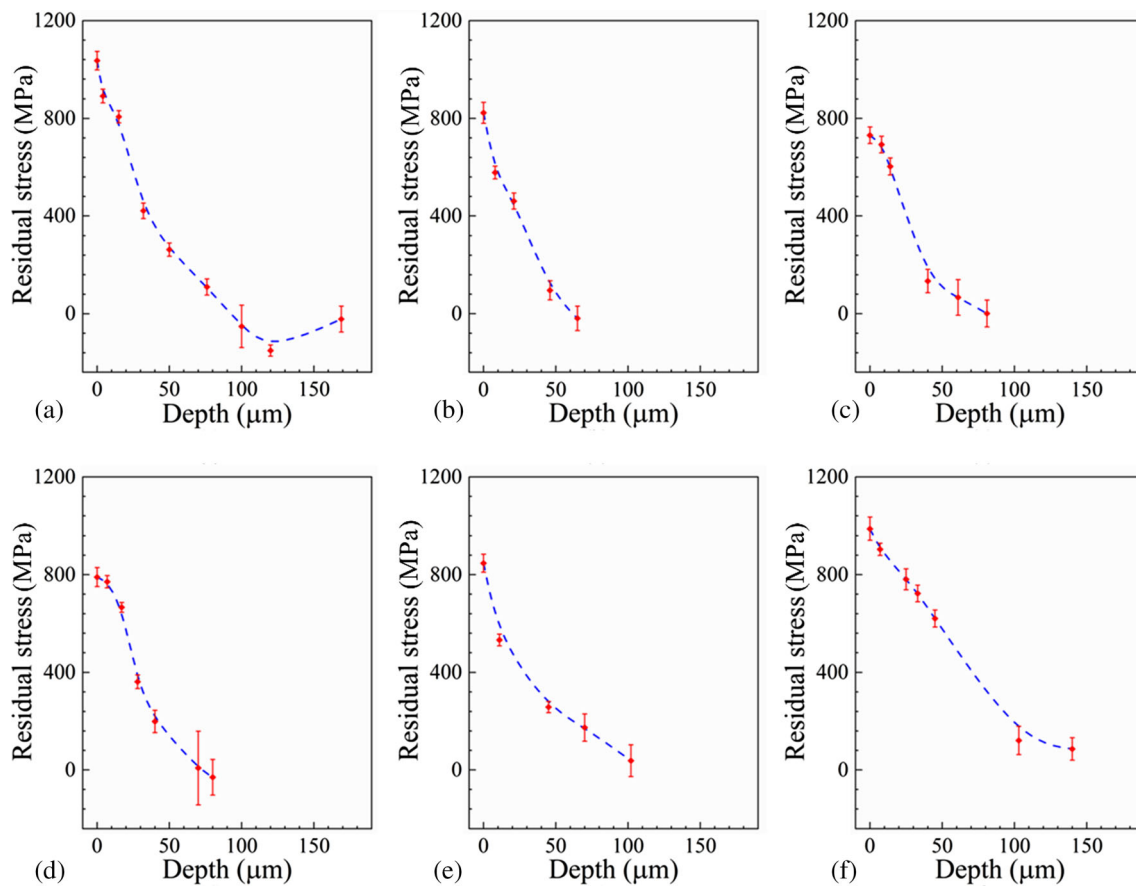


Fig. 2 Measured residual stress profiles: (a) specimen C1-1; (b) specimen C2-1; (c) specimen C3-1; (d) specimen C4-1; (e) specimen C5-1; (f) specimen C6-1. The dashed lines are fitted for the experimental data. The error bar represents standard deviation

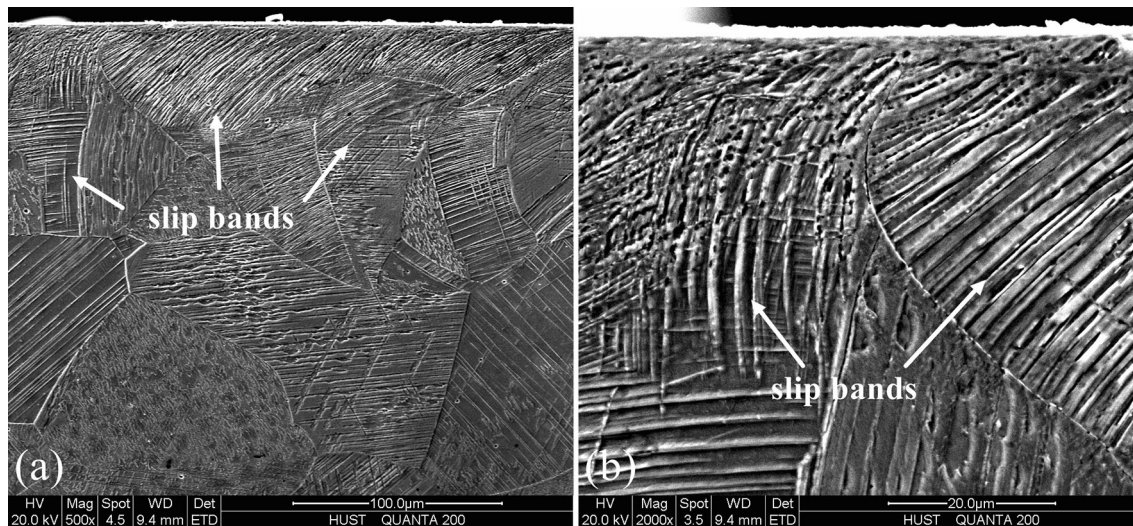


Fig. 3 Subsurface micromorphology of the specimen C1-2: (a) within 250 μm from the surface; (b) within 50 μm from the surface

observed that the micro-cracks inclined to develop along the slip bands after crossing the ultrafine-grain zone. Subsequently, the micro-crack could propagate with an inclination angle of about 45° to the slip band or develop from one slip plane to another. These observations revealed that the machining-induced slip bands had a great influence on the propagation of the micro-crack in the SCC initiation stage.

Moreover, the relation between the micro-crack growth and machining-induced microstructural changes was further investigated with EBSD. Figure 9 and 10 shows the EBSD results of the specimen C3-5 and C6-5, respectively, which had been subjected to the SCC test for 10 h. The detected zones covered a depth of 180 μm . The IPF, GB and KAM maps in Fig. 9 and 10 present a similar gradient of the microstructural changes as

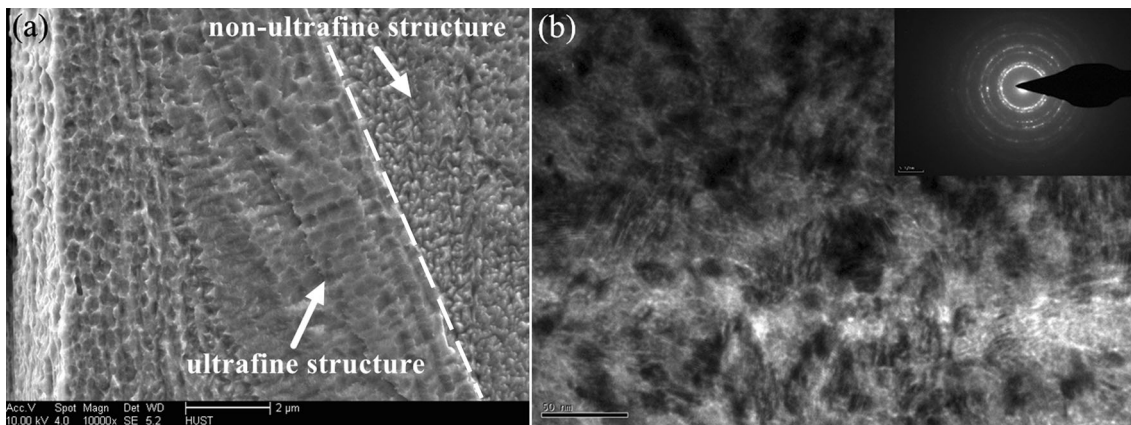


Fig. 4 Ultrafine-grain structure in the top surface zone of the specimen C2-2: (a) SEM result and (b) TEM result

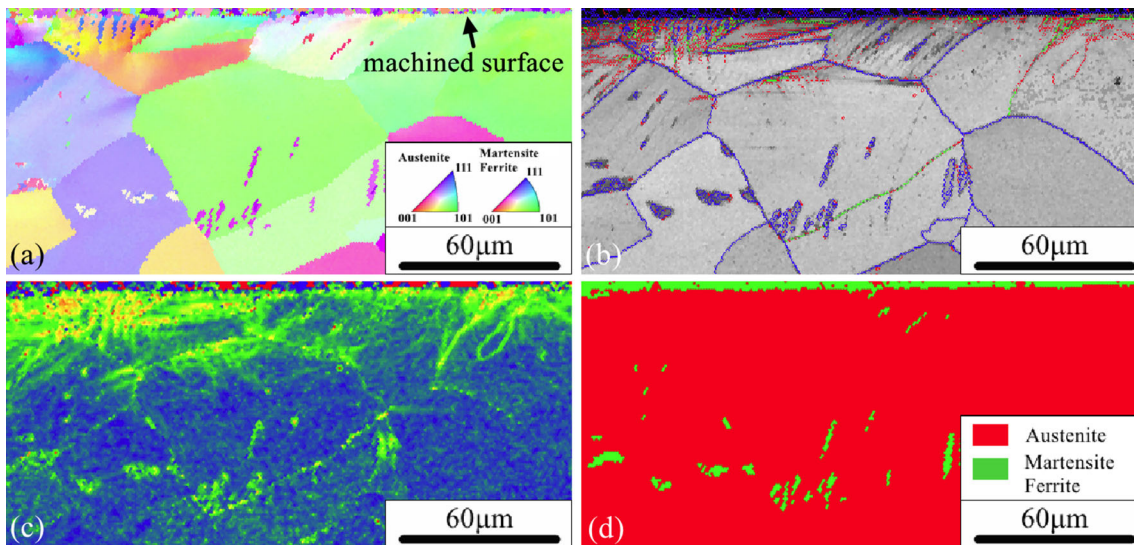


Fig. 5 EBSD results of the specimen C5-2 showing the subsurface microstructural changes: (a) IPF map, (b) GB map, (c) KAM map and (d) phase map

specimen C5-2, including the orientation variation, newly produced GBs and local dislocations. The extent of orientation variation, GB density and local deformation gradually decreased with the increase in depth.

In the IQ background GB maps, it was shown that the micro-cracks propagated through the gradient of the subsurface microstructures from the machined surface to the internal material. Five micro-cracks are shown in Fig. 9. The micro-cracks were observed to be transgranular (TG), with depths ranging from 34 to 125 μm . Besides, Fig. 10 displays six micro-cracks ranging from 31 to 109 μm in depth. Except for crack 3, the observed cracks were TG micro-cracks. In particular, crack 6 was developed from an intergranular (IG) micro-crack. From Fig. 9 and 10, the SCC micro-cracks were noted to be initiated from the near-surface zone, where the orientation change was prominent, and the GB density as well as dislocation density were at a high level. Finally, the SCC micro-cracks would be arrested in the subsurface, where the orientation change was negligible, and the GBs and dislocations were barely detectable.

Table 4 lists the micro-crack depth as a function of exposure time for condition C1. For the specimens C1-2, C1-3 and C1-4, tested in boiling MgCl_2 solution for 30, 60 and 300 min, the

average micro-crack depths were observed to be 78.4, 64.1 and 77.1 μm , respectively. The observed maximum depth was about 150–160 μm . The results demonstrated that the micro-crack depths remained almost at the same level. The relationship between the micro-crack depth and the test duration indicated that the micro-crack propagation into the material mainly occurred in the first 30 min in the boiling MgCl_2 solution.

In addition, Table 5 presents the comparison of the micro-crack depth of the specimens C1-5, which had been exposed to the SCC environment for 600 min. The average micro-crack depths of conditions C1-6 were noted to be 77.1, 56.2, 45.9, 56.7, 78.4 and 94.2 μm , while the maximum depths were 166.7, 155.7, 125.7, 132.4, 196.8 and 248.4 μm , respectively.

4. Discussion

4.1 Effects of the Residual Stress

Our previous investigation revealed a strong relation between the residual tensile stress and SCC micro-crack

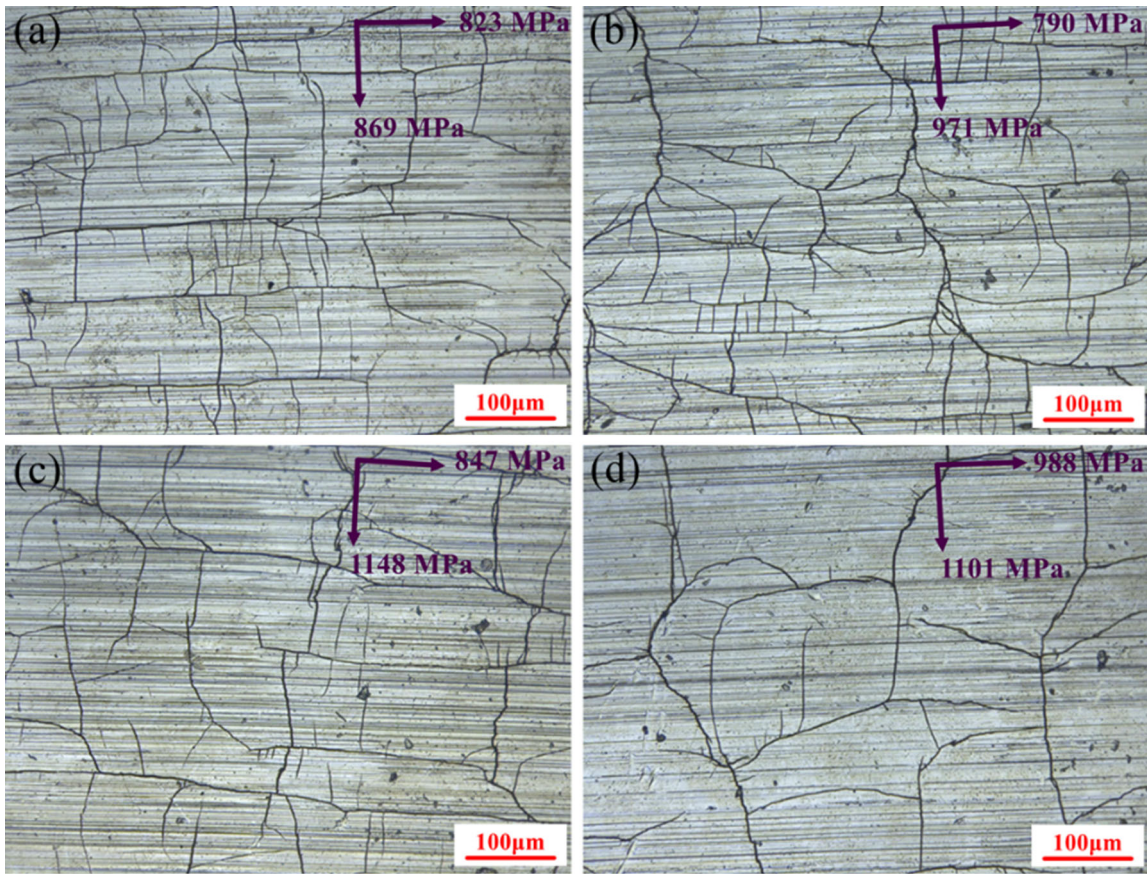


Fig. 6 SCC micro-crack morphology on machined surface: (a) C2-3, (b) C4-3, (c) C5-3, (d) C6-3

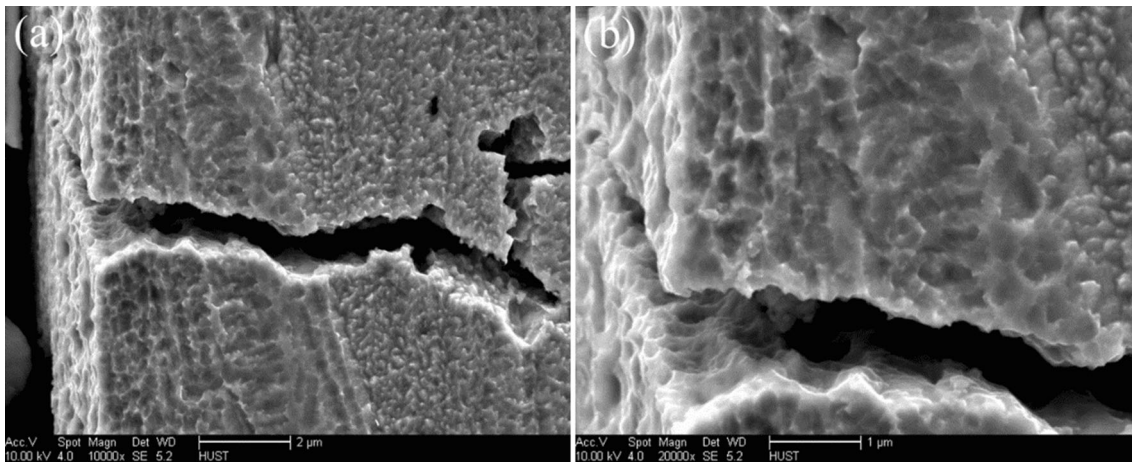


Fig. 7 FSEM images showing the micro-crack initiated in the surface ultrafine-grain layer

initiation on the milled surface of 316 ASS (Ref 14). In the study, the surface residual stress in the machining direction was observed to be much higher than the transverse direction. Accordingly, the micro-crack initiation in the transverse direction was prominent, while it was not obvious in the machining direction. In the present study, the turning operations introduced large tensile residual stresses in both cutting and transverse directions. As a result, the micro-cracks were initiated in both directions, presenting a crisscrossing meshwork morphology. Moreover, the results revealed that the SCC

initiation was significant on the machined surfaces, while it was not observed on the polished surface. This comparison highlights the role of the machining-induced residual stress in the SCC initiation.

Further, the effect of the residual stress on the SCC micro-crack propagation in the machined subsurface was explored. The occurrence frequency of the observed crack depth in the specimens Ci-5 is shown in Fig. 11. The crack depth distribution was compared with the residual stress profile (shown in Fig. 2), and the results presented a significant observation that the depth

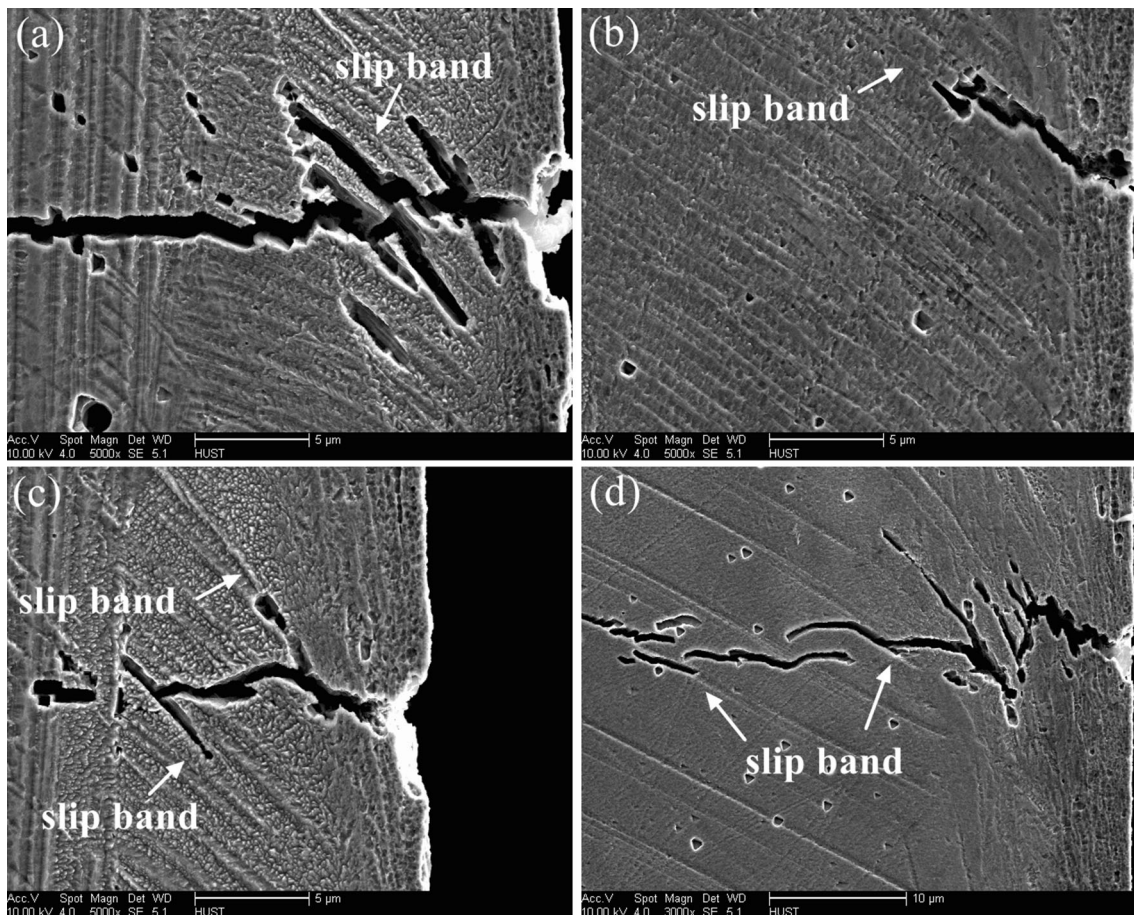


Fig. 8 FSEM images showing that the machining-induced slip bands had a strong correlation with micro-crack initiation

range corresponded to the zone with the residual stress lower than 200 MPa. For instance, for the specimen C1-5, most of the SCC micro-cracks were arrested in the depth range 60-130 μm , while the residual stress was reduced to 200 MPa at a depth of 60 μm . This phenomenon demonstrated high relevance between the residual stress level and SCC propagation.

Moreover, the average micro-crack depth of the specimens C1-5 was compared with the depth at which the residual stress was reduced to lower than 200 MPa (DP₂₀₀). The DP₂₀₀ values were derived from the residual stress profile as shown in Fig. 2. The comparison result, shown in Fig. 12, revealed that DP₂₀₀ was slightly lower than the average micro-crack depth in conditions C1-5, while it was slightly higher in C6. The resulting correlation between DP₂₀₀ and average micro-crack depth suggested that the micro-cracks would not propagate in case the residual stress was less than 200 MPa. It has been reported that there exists a critical residual stress, about 190 MPa, for the SCC initiation on the milled surface of 316 ASS (Ref 14). The machining-induced residual stress was concluded to be the essential driving force for developing the SCC micro-crack. A sufficiently large residual stress would not only cause the SCC initiation on the machined surface, but could also result in the SCC propagation in the subsurface. Therefore, the propagation of the SCC micro-cracks into the material was terminated due to the lack of the driving force. The DP₂₀₀ value can act as a critical depth for evaluating the SCC micro-crack growth in the machined subsurface of 304 ASS.

4.2 Effect of Microstructural Changes

The SCC initiation was affected not only by the residual stresses but also by the microstructural changes. Resulting from the plastic deformation introduced by machining, the generations of phase change, new GBs and slip bands were the major characteristics of the microstructural changes in the subsurface, as shown in Sect. 3.2. A quantitative analysis was performed to explore the correlation between the SCC micro-crack propagation and the microstructural changes.

The machining-induced microstructural changes were quantitatively characterized by the variation of the GB density and KAM values. The variation of GBs and KAM values with the subsurface depth is shown in Fig. 13. For most cases, the densities of LAGB, TAGB and HAGB decreased along the depth. Similarly, the KAM values also presented a monotonically decreasing trend. The KAM values decreased to a stable level where the machining-induced GB densities were retained in a stable state. A reduction in the HAGB density along the subsurface depth suggested that the fragmentation of the original grains was gradually reduced, and the reducing KAM values signified a reduction in the local deformation level.

Further, for the specimens exposed to boiling MgCl₂ solution for 600 min, the variation of the microstructural changes was compared with the crack depth, as shown in Fig. 13. Evidently, for all cases, the average crack depth was slightly higher than the depth for which the GB density and

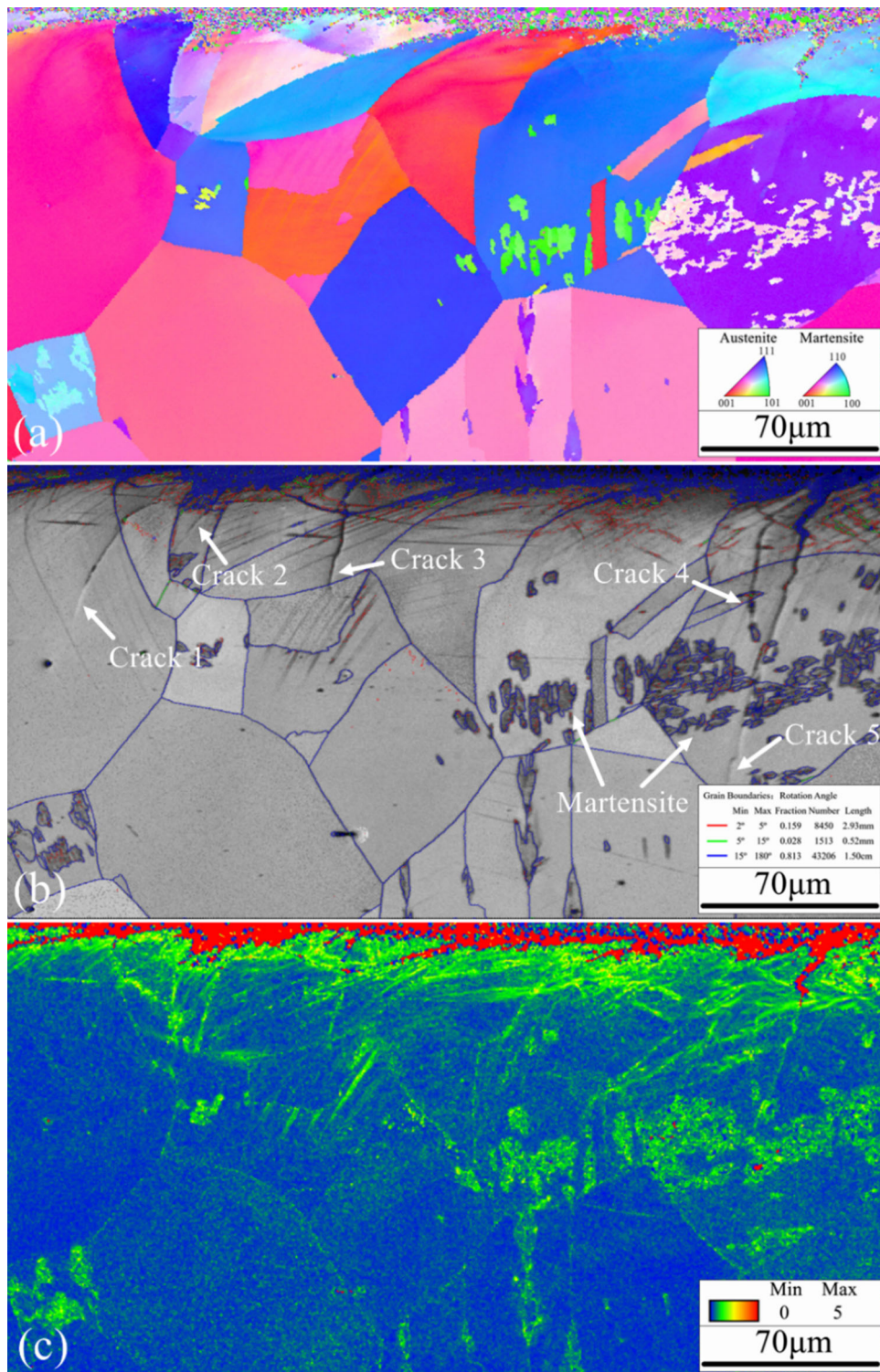


Fig. 9 EBSD analysis of the micro-cracks with the machining-induced microstructural changes of the specimen C3-5. (a) IPF map showing the crystal orientation changes. (b) GB map displaying the distributions of LAGB, TAGB and HAGB. (c) KAM map illustrating the local dislocation distribution

KAM value decreased to a stable level. This phenomenon indicated that the micro-cracks could propagate through the highly deformed zones where the GB density and local deformation were at a high level. Thus, it is concluded that the initiation and propagation of the SCC micro-cracks are related to the GBs and local deformation.

In addition, it was observed that the machining-induced slip bands correlated strongly with the development of the SCC micro-cracks, as shown in Fig. 8. The phenomena coincided with the reports of Magnin et al. (Ref 31) and Flanagan et al. (Ref 32), indicating that the SCC cracks would develop along the slip plane in the face-centered cubic crystal structures. This

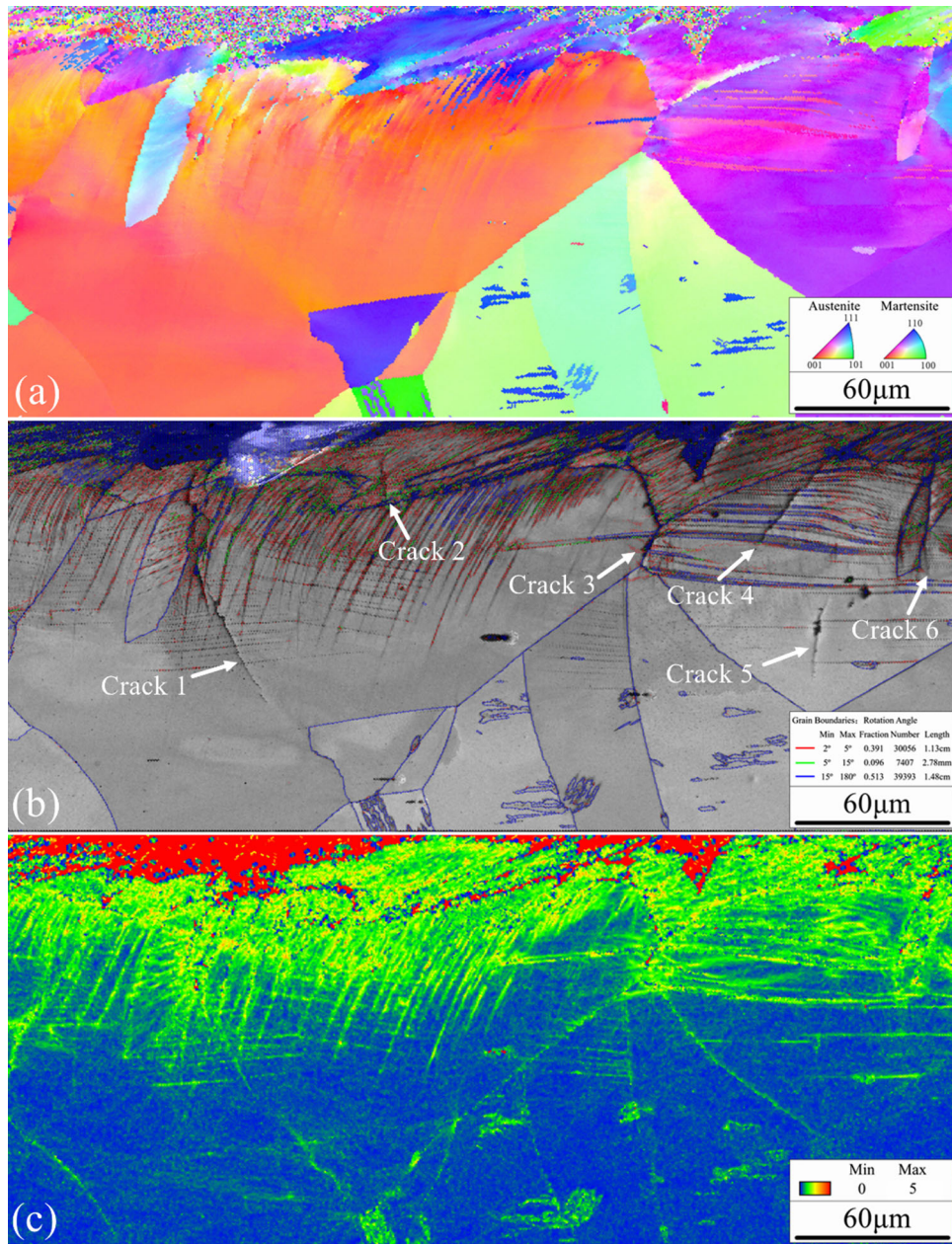


Fig. 10 EBSD analysis of the micro-cracks and machining-induced microstructural changes of the specimen C6-5. (a) IPF map showing the crystal orientation changes. (b) GB map displaying the distributions of LAGB, TAGB and HAGB. (c) KAM map illustrating the local dislocation distribution

Table 4 Micro-crack depth for C1 with different exposure time

Specimen	Corrosion time, min	Micro-crack number	Crack depth, μm	
			Average	Maximum
C1-3	30	18	78.4	147.7
C1-4	60	15	64.1	159.3
C1-5	600	32	77.1	166.7

can be explained by the preferential dissolution/attack along the slip band, where the fresh metal was exposed to the corrosion environment during the SCC process (Ref 10). The slip band is

composed of several slip planes, which have the highest atomic density and are considered as the closed packed planes. The slip resistance between such planes is relatively low, and thus the

crystal easily cracks along the slip bands. Therefore, the slip bands in the machined subsurface have a significant influence on the development of the SCC micro-cracks.

4.3 Characterization Model of Machined Subsurface and SCC Sensitivity

According to the resulting distributions of the residual stress and microstructural changes, the residual stresses penetrated in the subsurface were coupled with a gradient of the microstructure alterations along the subsurface. The depth range of the machining-induced GBs was measured with EBSD and compared with the DP₂₀₀ value. Figure 14 displays the comparison between the DP₂₀₀ values and depth range of the machining-induced GBs. Interestingly, the comparison indicated that the machining-induced GBs zone corresponded to the depth where the residual stress was higher than 200 MPa.

On the basis of the observed results, a characterization model of machined subsurface and SCC sensitivity was proposed. The subsurface deformed zone could be classified into four layers from the surface to the interior, as shown in

Table 5 Micro-crack depth for the specimen Ci-5 with the exposure time of 600 min

Specimen	Micro-crack number	Crack depth, μm	
		Average	Maximum
C1-5	32	77.1	166.7
C2-5	41	56.2	155.7
C3-5	23	45.9	125.7
C4-5	48	56.7	132.4
C5-5	37	78.4	196.8
C6-5	61	94.2	248.4

Fig. 15. The uppermost layer is the ultrafine-grain layer, as clarified in Fig. 4. The next layer is the broken layer where the original grains are split at the microscale. A large number of HAGBs are generated in both the ultrafine-grain and the broken layers. The seriously deformed layer is beneath the broken layer with the prominent appearance of LAGBs and slip bands. The last layer is the slightly deformed one where no obvious GBs are produced; however, some minor orientation changes still exist. Under the slightly deformed layer is the non-deformed base material. This implies that the ultrafine-grain, broken and seriously deformed layers are suffered a residual tensile stress higher than 200 MPa, while the residual stress of the slightly deformed layer is lower than 200 MPa or in the compressive state.

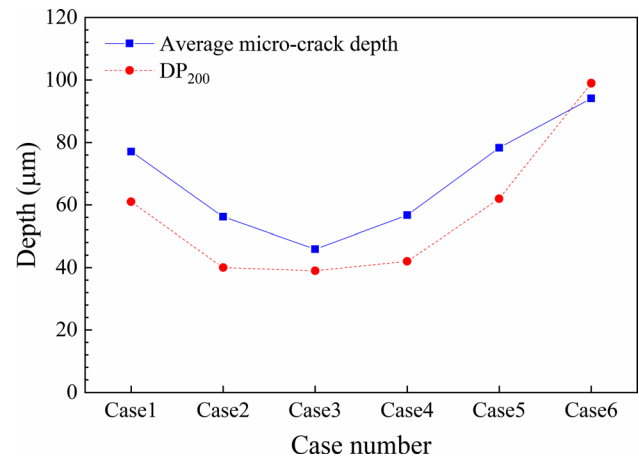


Fig. 12 Comparison of the average micro-crack depth with the DP₂₀₀

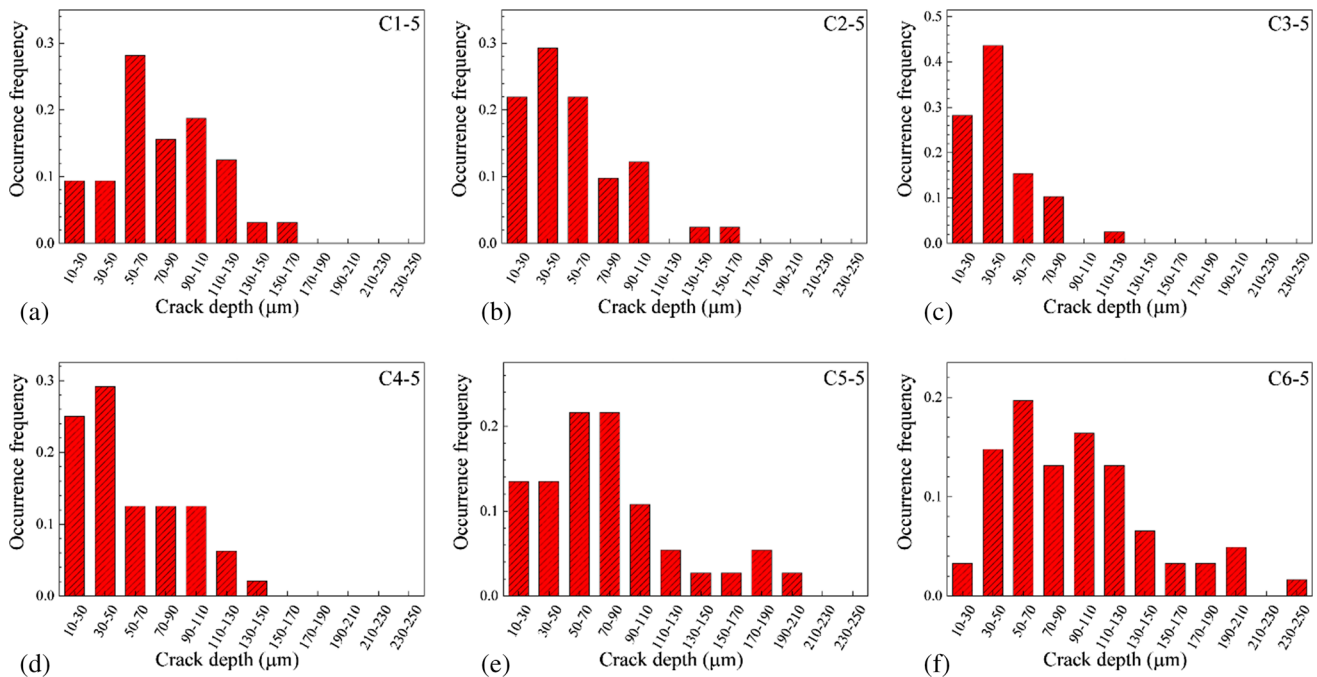


Fig. 11 Micro-crack depth distribution of the specimens Ci-5

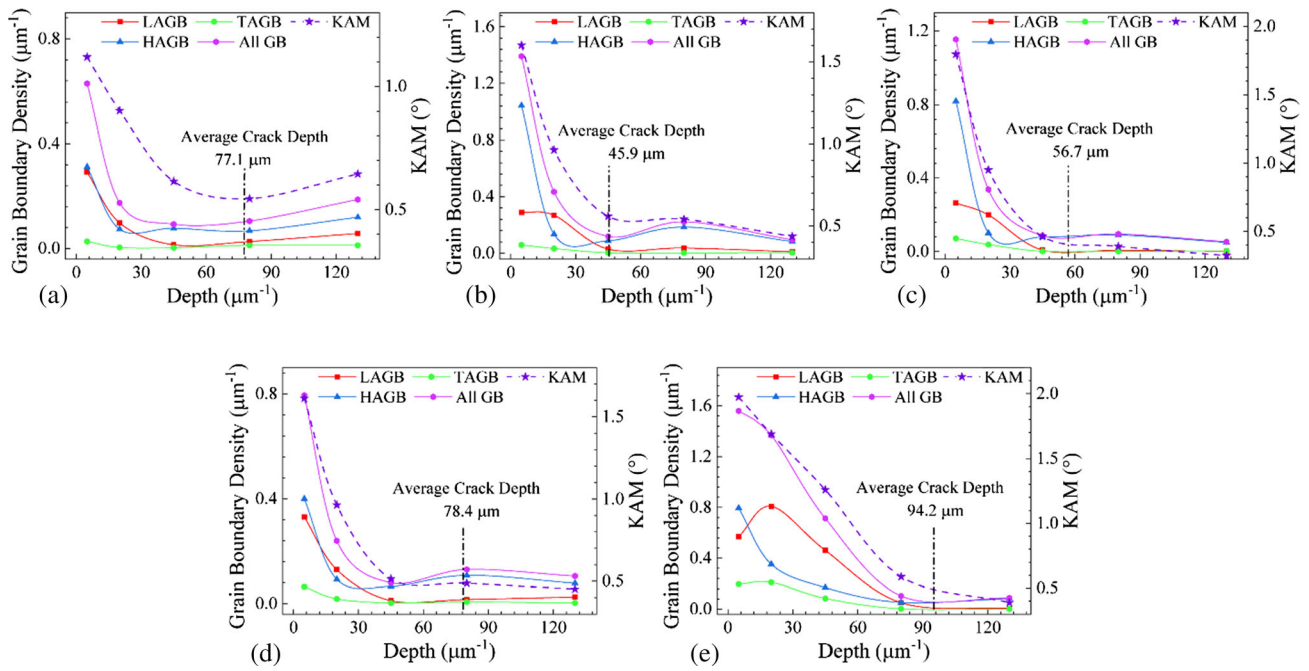


Fig. 13 Variations of GBs and KAM with the depth: (a) C1, (b) C3, (c) C4, (d) C5, (e) C6

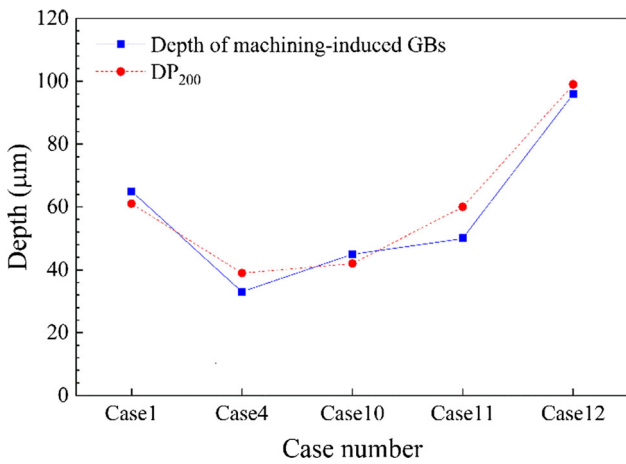


Fig. 14 Comparison of the depth of machining-induced GBs with the DP_{200}

As shown in Fig. 15, the machining process introduces a large residual stress on the machined surface. As the surface is exposed to the corrosion environment, the SCC micro-crack would be initiated on the machined surface in the direction perpendicular to the residual tensile stress and subsequently developed into the material. In the subsurface, the SCC micro-crack propagates through the near-surface ultrafine-grain, broken and seriously deformed layers where high SCC sensitivity is retained. Finally, the SCC micro-crack would be arrested in the slightly deformed layer. Accordingly, the subsurface zone with high SCC sensitivity is identified. The SCC micro-crack is prone to develop in the subsurface zone

where the residual stress is larger than 200 MPa, along with high-density GB.

5. Conclusions

The initiation and propagation of the SCC micro-crack were associated with the gradients of the machining-induced residual stresses and microstructural changes in the subsurface of 304 ASS. The main conclusions can be drawn as follows:

1. The zone of high SCC sensitivity in the machined subsurface is identified. The SCC micro-crack was prone to develop in the subsurface where the residual stress was larger than 200 MPa, along with high-density GB. The high residual stress, accumulation of dislocations and appearance of slip bands were responsible for an increment in the SCC sensitivity.
2. In the machined subsurface, the majority of the micro-cracks were arrested where the residual stress was reduced to lower than 200 MPa. The DP_{200} value acted as a critical depth for evaluating the growth of the residual stress-induced micro-crack.
3. In the machined subsurface, the propagation of the micro-crack terminated where the local deformation and machining-induced GBs were negligible. The early SCC micro-cracks in the initiation stage mainly extended along the slip bands.
4. The machining-induced microstructural changes were closely related to the residual stress. The subsurface zone with the high fraction of HAGB, TAGB and LAGB corresponded to the depth where the residual stress was greater than 200 MPa.

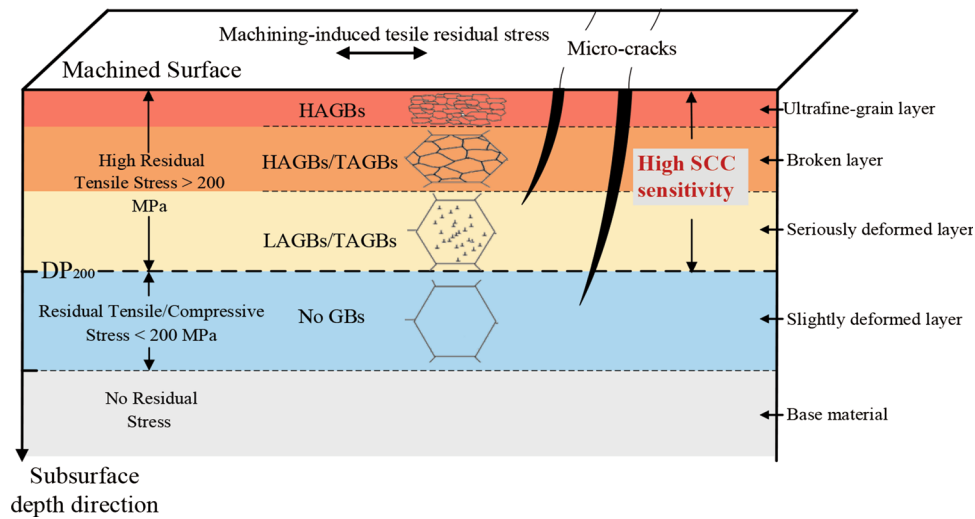


Fig. 15 Schematic of micro-crack development on the cross section associated with the machining-induced residual stress and microstructural changes

Acknowledgments

This work is supported by the National Natural Science Foundation of China (Grant No. 51875219, 51375182). The authors thank Analytical and Testing Center of HUST for FSEM and TEM measurements and Advanced Manufacturing and Technology Experiment Center of School of Mechanical Science and Engineering of HUST for residual stress measurements.

References

- D. Merezhko, M. Merezhko, M. Gushev, J. Busby, O. Maksimkin, M. Short, and F. Garner, *Investigation of Pitting Corrosion in Sensitized Modified High-Nitrogen 316LN Steel After Neutron Irradiation, Environmental Degradation of Materials in Nuclear Power Systems*, Springer, Berlin, 2017, p 1125–1140
- O.M. Alyousif and R. Nishimura, The Effect of Test Temperature on SCC Behavior of Austenitic Stainless Steels in Boiling Saturated Magnesium Chloride Solution, *Corros. Sci.*, 2006, **48**(12), p 4283–4293
- D.T. Spencer, M.R. Edwards, M.R. Wenman, C. Tsitsios, G.G. Scatigno, and P.R. Chard-Tuckey, The Initiation and Propagation of Chloride-Induced Transgranular Stress-Corrosion Cracking (TGSCC) of 304L Austenitic Stainless Steel Under Atmospheric Conditions, *Corros. Sci.*, 2014, **88**, p 76–88
- O.M. Alyousif and R. Nishimura, The Stress Corrosion Cracking Behavior of Austenitic Stainless Steels in Boiling Magnesium Chloride Solutions, *Corros. Sci.*, 2007, **49**(7), p 3040–3051
- J.P. Davim, *Surface Integrity in Machining*, Springer, Berlin, 2010
- A. Turnbull, K. Mingard, J.D. Lord, B. Roebuck, D.R. Tice, K.J. Mottershead, N.D. Fairweather, and A.K. Bradbury, Sensitivity of Stress Corrosion Cracking of Stainless Steel to Surface Machining and Grinding Procedure, *Corros. Sci.*, 2011, **53**(10), p 3398–3415
- S. Ghosh and V. Kain, Effect of Surface Machining and Cold Working on the Ambient Temperature Chloride Stress Corrosion Cracking Susceptibility of AISI, 304L Stainless Steel, *Mater. Sci. Eng. A*, 2010, **527**(3), p 679–683
- S.G. Acharyya, A. Khandelwal, V. Kain, A. Kumar, and I. Samajdar, Surface Working of 304L Stainless Steel: Impact on Microstructure, Electrochemical Behavior and SCC Resistance, *Mater. Charact.*, 2012, **72**, p 68–76
- N. Zhou, R. Lin Peng, R. Pettersson, M. Schönning, Residual Stress in Stainless Steels After Surface Grinding and its Effect on Chloride Induced SCC, in International Conference on Residual Stresses, 3–7 July 2016, Sydney, Australia, 2016, pp. 289–294
- S. Ghosh and V. Kain, Microstructural Changes in AISI, 304L Stainless Steel Due to Surface Machining: Effect on its Susceptibility to Chloride Stress Corrosion Cracking, *J. Nucl. Mater.*, 2010, **403**(1), p 62–67
- T. Shoji, Progress in the Mechanistic Understanding of BWR SCC and its Implication to Prediction of SCC Growth Behavior in Plants, in 11th International Symposium on Environmental Degradation of Materials in Nuclear Power Systems-Water Reactors, 2003 (Stevenson Washington, USA), NACE
- O. Raquet, E. Herms, F. Vaillant, and T. Couvant, SCC of Cold-Worked Austenitic Stainless Steels in PWR Conditions, *Adv. Mater. Sci.*, 2007, **7**(1), p 33–46
- L. Chang, J. Duff, M.G. Burke, F. Scenini, SCC Initiation in the Machined Austenitic Stainless Steel 316L in Simulated PWR Primary Water, in Environmental Degradation of Materials in Nuclear Power Systems, 2017, Springer, pp 811–827
- W. Zhang, K. Fang, Y. Hu, S. Wang, and X. Wang, Effect of Machining-Induced Surface Residual Stress on Initiation of Stress Corrosion Cracking in 316 Austenitic Stainless Steel, *Corros. Sci.*, 2016, **108**, p 173–184
- H. Wu, C. Li, K. Fang, F. Xue, G. Zhang, K. Luo, and L. Wang, Effect of Machining on the Stress Corrosion Cracking Behavior in Boiling Magnesium Chloride Solution of Austenitic Stainless Steel, *Mater. Corros.*, 2018, **69**(4), p 519–526
- S. Ghosh, V.P.S. Rana, V. Kain, V. Mittal, and S.K. Baveja, Role of Residual Stresses Induced by Industrial Fabrication on Stress Corrosion Cracking Susceptibility of Austenitic Stainless Steel, *Mater. Des.*, 2011, **32**(7), p 3823–3831
- N. Zhou, R. Pettersson, R.L. Peng, and M. Schönning, Effect of Surface Grinding on Chloride Induced SCC of 304L, *Mater. Sci. Eng. A*, 2016, **658**, p 50–59
- A. BenRhouma, H. Sidhom, C. Braham, J. Lédion, and M.E. Fitzpatrick, Effects of Surface Preparation on Pitting Resistance, Residual Stress, and Stress Corrosion Cracking in Austenitic Stainless Steels, *J. Mater. Eng. Perform.*, 2001, **10**(5), p 507–514
- A. Grabulov, R. Petrov, and H.W. Zandbergen, EBSD Investigation of the Crack Initiation and TEM/FIB Analyses of the Microstructural Changes Around the Cracks Formed Under Rolling Contact Fatigue (RCF), *Int. J. Fatigue*, 2010, **32**(3), p 576–583
- Y. Motoyashiki, A. Brückner-Foigt, and A. Sugeta, Microstructural Influence on Small Fatigue Cracks in a Ferritic–Martensitic Steel, *Eng. Fract. Mech.*, 2008, **75**(3), p 768–778
- W. Zhang, X. Wang, Y. Hu, and S. Wang, Quantitative Studies of Machining-Induced Microstructure Alteration and Plastic Deformation in AISI, 316 Stainless Steel Using EBSD, *J. Mater. Eng. Perform.*, 2018, **27**(2), p 434–446
- L. Zhu, Y. Yan, J. Li, L. Qiao, Z. Li, and A.A. Volinsky, Stress Corrosion Cracking at Low Loads: Surface Slip and Crystallographic Analysis, *Corros. Sci.*, 2015, **100**, p 619–626

23. L.J. Qiao, K.W. Gao, A.A. Volinsky, and X.Y. Li, Discontinuous Surface Cracks During Stress Corrosion Cracking of Stainless Steel Single Crystal, *Corros. Sci.*, 2011, **53**(11), p 3509–3514
24. J.C. Fisher, E.W. Hart, and R.H. Pry, Theory of Slip-Band Formation, *Phys. Rev.*, 1952, **87**(6), p 958
25. T. Magnin, A. Chambreuil, and B. Bayle, The Corrosion-Enhanced Plasticity Model for Stress Corrosion Cracking in Ductile FCC Alloys, *Acta Mater.*, 1996, **44**(4), p 1457–1470
26. J.C. Outeiro, D. Umbrello, and R. M'Saoubi, Experimental and Numerical Modelling of the Residual Stresses Induced in Orthogonal Cutting of AISI, 316L Steel, *Int. J. Mach. Tools Manuf.*, 2006, **46**(14), p 1786–1794
27. F. Valiorgue, J. Rech, H. Hamdi, P. Gilles, and J.M. Bergheau, 3D Modeling of Residual Stresses Induced in Finish Turning of an AISI304L Stainless Steel, *Int. J. Mach. Tools Manuf.*, 2012, **53**(1), p 77–90
28. R. Petrov, L. Kestens, A. Wasilkowska, and Y. Houbaert, Microstructure and Texture of a Lightly Deformed TRIP-Assisted Steel Characterized by Means of the EBSD Technique, *Mater. Sci. Eng. A*, 2007, **447**(1), p 285–297
29. H. Gao, Y. Huang, W.D. Nix, and J.W. Hutchinson, Mechanism-Based Strain Gradient Plasticity—I. Theory, *J. Mech. Phys. Solids*, 1999, **47**(6), p 1239–1263
30. “ASTM G36-94,” American Society for Testing and Materials (2006)
31. T. Magnin, R. Chieragatti, and R. Oltra, Mechanism of Brittle Fracture in a Ductile 316 Alloy During Stress Corrosion, *Acta Metall. Mater.*, 1990, **38**(7), p 1313–1319
32. W.F. Flanagan, P. Bastias, and B.D. Lichter, A Theory of Transgranular Stress-Corrosion Cracking, *Acta Metall. Mater.*, 1991, **39**(4), p 695–705

Publisher's Note Springer Nature remains neutral with regard to jurisdictional claims in published maps and institutional affiliations.